ACS Catalysis

Research Article

Cite This: ACS Catal. 2018, 8, 1532−1545

pubs.acs.org/acscatalysis

# NiSx Quantum Dots Accelerate Electron Transfer in $Cd_{0.8}Zn_{0.2}S$ Photocatalytic System via an rGO Nanosheet "Bridge" toward Visible-Light-Driven Hydrogen Evolution

Chao Xue, He Li, Hua An, Bolun Yang, Jinjia Wei, and Guidong Yang*

XJTU-Oxford Joint International Research Laboratory of Catalysis, School of Chemical Engineering and Technology, Xi'an Jiaotong University, Xi'an, Shaanxi 710049, People's Republic of China

Supporting Information

**ABSTRACT:** Minimizing the charge transfer barrier to realize fast spatial separation of photoexcited electron−hole pairs is of crucial importance for strongly enhancing the photocatalytic $H_2$ generation activity of photocatalysts. Herein, we propose an electron transfer strategy by reasonable design and fabrication of high-density NiSx quantum dots (QDs) as a highly efficient cocatalyst on the surface of $Cd_{0.8}Zn_{0.2}S$/rGO nanosheet composites. Under visible-light irradiation, the formation of a two-dimensional (2D) $Cd_{0.8}Zn_{0.2}S$/rGO nanohybrid system with 2 wt % NiSx loading gave a prominent apparent quantum efficiency (QE) of 20.88% (435 nm) and $H_2$ evolution rate of 7.84 mmol $g^{-1}$ $h^{-1}$, which is 1.4 times higher than that of Pt/$Cd_{0.8}Zn_{0.2}S$/rGO. It is believe that the introduced rGO nanosheets and NiSx QDs obviously improved the interfacial conductivity and altered the spatial distribution of electrons in this nanoarchitecture. Thus, the synergistic effects of interfacial junctions result in a regulated electron transportation pathway along the basal planes and ultrafast transfer and spatial separation of photoexcited carriers, which are responsible for the enhanced photocatalytic performance. This work gives a facile and effective strategy to understand and realize rationally designed advanced photocatalysts for high-efficiency, stable, and cost-efficient solar hydrogen evolution applications.

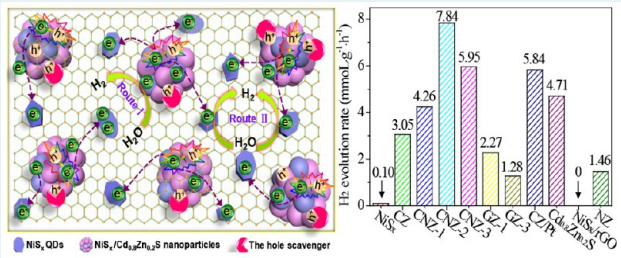


**KEYWORDS:** *$Cd_{0.8}Zn_{0.2}S$/rGO, NiSx, quantum dot, nanosheet, hydrogen evolution*

## 1. INTRODUCTION

Direct solar water splitting for hydrogen production over an efficient photocatalyst is one of the most important pathways to generate clean, renewable, and carbon-neutral alternative $H_2$ fuel on a large scale.[1,2] To date, extensive studies on semiconductor photocatalysts have found that an appropriate cocatalyst, especially noble metals such as Pt, Ru, and Pd, can assist in significantly improving photocatalytic $H_2$ evolution from water splitting, because these aforementioned cocatalysts not only promote the interfacial charge transfer and separation but also can serve as highly surface reactive sites to reduce the activation energy or the overpotential of the $H_2$ evolution reaction.[3−6] However, the higher cost and the low photochemical conversion efficiency of these noble-metal cocatalysts remain the main shortcomings that limit the practical implementation of photocatalytic $H_2$ evolution. To address these bottleneck issues, the exploitation of cost-effective and robust cocatalysts with high photocatalytic activity and stability has become the most efficient strategy to enhance the photocatalytic activity of $H_2$ generation. Among these alternative cocatalysts, transition-metal chalcogenides, such as $MoS_2$,[7−10] $WS_2$,[11−13] NiS,[14] $Sb_2S_3$,[15] $W_xMo_{1-x}S_2$,[16] and CoS,[17,18] are believed to be promising substitutes for traditional Pt-group metals due to their low cost, long-term chemical stability, ultrahigh charge carrier mobility, and high efficiency. In particular, the development of NiSx cocatalysts that can be used for a cost-effective and high-efficiency $H_2$ evolution system is significantly favored, due to their low cost and earth-abundant elements. Most importantly, NiSx displays the lowest activation energy in forming a Ni−H bond with the surface-adsorbed $H_2O$ during proton reduction in comparison with other non-noble-metal species.[19] This behavior will facilitate the adsorption−reduction−desorption process of hydrogen, thus dramatically enhancing the photocatalytic $H_2$ evolution reaction.[4]

In recent years, more and more endeavors have been devoted to the synthesis of highly active graphene-based photocatalysts decorated by cost-effective cocatalyst quantum dots (QDs), owing to their advantageous optical and electronic properties.[20,21] As it is well-known that graphene oxide (GO) has some intrinsic advantages, such as excellent conductivity, good flexibility, ultrahigh electron mobility, and large specific surface area,[22−25] it can serve as an unconventional soft material for the epitaxial growth of hybrid nanostructures through incorpo-

Received: December 10, 2017
Revised: January 4, 2018
Published: January 4, 2018

ACS Publications © 2018 American Chemical Society



DOI: 10.1021/acscatal.7b04228
ACS Catal. 2018, 8, 1532−1545

ration of diversified semiconductors. In this regard, a $Cd_xZn_{1-x}S$ ternary chalcogenide solid solution, as an n-type narrow-band-gap semiconductor with good photocatalytic performance and stability, can act as a favorable candidate for building nanohybrid nanostructures on an ultrathin graphene nanosheet.[26−28] Most importantly, this kind of material possesses a tunable band gap position just by adjusting the component ratio of cadmium to zinc. However, even with so many structural and performance advantages, both the quantum efficiency and the solar energy conversion efficiency of either the pure $Cd_xZn_{1-x}S$ solid solution substance or the binary graphene-based nanocomposite are still very low for practical applications because of the sluggish transfer of photoinduced charge carrier and external energy loss during long-distance transportation between the separated photoabsorbers and reactive site centers.[29−33] Therefore, there is a great amount of room for further improvement of its photocatalytic efficiency by shortening the distance of charge migration as well as fast spatial separation of the photoexcited electron−hole pairs. Previous studies have revealed that the decoration of quantum-sized cocatalysts onto the aforementioned graphene-based nanohybrids is of great importance in their complex surface electron distribution,[31,34] which is considered to be one of the most efficient strategies to not only greatly improve the separation and migration of the charge carriers but also increase the surface $H_2$-evolution active sites, thus significantly boosting the photocatalytic activity of the novel visible-light-driven photocatalytic $H_2$ evolution system.[35,36]

Motivated by the above consideration, in this work we report a rational design and self-assembly synthesis of mesoporous $Cd_{0.8}Zn_{0.2}S$ nanospheres with precise interfacial boundary homogeneously in-plane epitaxial growth on a reduced graphene oxide (rGO) surface, accompanying the uniform dispersion of NiSx QDs on the surfaces of both $Cd_{0.8}Zn_{0.2}S$ and rGO by a facile hydrothermal method. Our strategy for preparing the NiSx/$Cd_{0.8}Zn_{0.2}S$/rGO nanocomposite synergistically extends the light absorption and modulates the surface electron spatial distribution characteristics when the photocatalytic $H_2$ production is performed. Therefore, this unconventional nanohybrid system shows a remarkable apparent QE of 20.88% (435 nm) and the high reaction rate of 7.84 mmol $g^{-1}$ $h^{-1}$. In addition, given their specific structural features, preeminent photocatalytic activity and stability, and promising applications, a firm correlation between the accelerated charge transfer dynamics and unique structural properties was evidenced by tangible experimental proof. This work could inspire ongoing interest in an in-depth understanding of the mechanism of spatial charge separation within 2D composite structures decorated by a new generation of cocatalysts and thus in the design of highly efficient, steady, and cost-effective solar energy conversion nanomaterials.

## 2. EXPERIMENTAL SECTION

**2.1. Synthesis of the Aqueous Dispersion of Graphene Oxide (GO) Nanosheets.** All chemicals were of analytical grade and were used without further purification. Graphite oxide was first prepared from natural flake graphite powder via a modified Hummer method.[37] Then, the obtained graphite oxide powder was exfoliated to GO nanosheets by an ultrasonic exfoliation method. Typically, 60 mg of graphite oxide powder and 20 mL of deionized water were placed in a 50 mL reagent tube. The graphite oxide suspension was ultrasonicated for 6 h in an ice bath by an Ultrasonic Cell Disruption System (JB500) with an output power of 520 W. Afterward, the resulting GO nanosheet dispersion (3 mg $mL^{-1}$) was settled for further use.

**2.2. Synthesis of the NiSx/$Cd_{0.8}Zn_{0.2}S$/rGO Nanosheet Composites.** NiSx/$Cd_{0.8}Zn_{0.2}S$-rGO nanosheet composites were fabricated through a facile one-pot hydrothermal method. In a typical synthesis, 5 mL of a 3 mg $mL^{-1}$ GO nanosheet dispersion was dispersed in 50 mL of deionized water by ultrasonication for 5 min. Subsequently, 0.06 g of $Zn(NO_3)_2 \cdot 6H_2O$, 0.18 g of $CdCl_2 \cdot 2.5H_2O$, 0.01 g of $Ni(NO_3)_2 \cdot 6H_2O$, and 0.2 g of glucose were added into 50 mL deionized water with magnetic stirring for 6 h. Then 0.54 g of L-cysteine was added into the above solution in turn with vigorous stirring for 1 h, and this mixture was then transferred into a 100 mL Teflon-lined stainless-steel autoclave and heated in an electric oven at 160 °C for 2 h. After the reaction mixture was cooled to room temperature, the resulting dark green product was centrifuged, washed several times with deionized water and absolute alcohol, and finally dried under vacuum at 60 °C for 12 h. For comparison, the binary $Cd_{0.8}Zn_{0.2}S$/rGO nanosheet composite was also prepared following the same procedure as that for NiSx/$Cd_{0.8}Zn_{0.2}S$/rGO nanocomposite in the absence of nickel compounds. In addition, the aforementioned procedures were used for the preparation of the pristine NiSx and $Cd_{0.8}Zn_{0.2}S$ nanostructures without the addition of GO, respectively.

**2.3. Characterization.** The crystal phase of the samples was analyzed by an X-ray diffractometer (XRD; Shimadzu, Lab X XRD-6100) with Cu K$\alpha$ radiation ($\lambda$ = 1.5418 Å). The morphologies, microstructures and elemental compositions of the samples were investigated by using a scanning electron microscope (FE-SEM, FEI Quanta F250, 200 kV) and a transmission electron microscope (TEM; JEOL, JEM-2100) equipped with an energy dispersive spectrometer (EDS). The $N_2$ adsorption and desorption isotherms were measured on a BET analyzer (BELSORP-Max, MicrotracBEL), and the specific surface area and pore size distribution were tested by the Brunauer−Emmett−Teller (BET) and Barrett−Joyner−Halenda (BJH) methods. The UV−vis diffuse reflection spectra were recorded on a UV-2600 UV−vis spectrophotometer (Shimadzu, Japan). The steady-state photoluminescence (PL) spectra and the time-resolved fluorescence decay spectra were surveyed by a steady-state/transient fluorescence spectrometer (Edinburgh Instruments, FLS980) with excitation and emission wavelengths at 325 and 470 nm at room temperature, respectively. Fourier transform infrared spectra (FT-IR) were recorded on a Nicolet iS50 spectrophotometer (ThermoFisher), and the Raman spectra were collected on a laser Raman spectrometer (HORIBA, LabRAM HR Evolution) with an excitation wavelength of 633 nm.

**2.4. Photocatalytic $H_2$ Evolution.** Visible-light-driven photocatalytic hydrogen evolution reactions were performed in a gas-closed system with a side irradiation Pyrex reaction cell at room temperature, which has an effective irradiation area of 12.56 $cm^2$. Briefly, 0.05 g of the photocatalyst was dispersed in 50 mL of deionized water that contained 5 mL of lactic acid as an electron donor. Then the solution was degassed with $N_2$ for 5 min to drive away the $O_2$ in the solution. A 300 W xenon lamp (HSX-F/UV300, *NBeT*) equipped with a UV-cutoff filter was used as the visible light source ($\lambda$ >420 nm). The $H_2$ production was evaluated by a gas chromatograph (SP-2100A, BFRL, Beijing; a thermal conductive detector equipped with a


DOI: 10.1021/acscatal.7b04228
ACS Catal. 2018, 8, 1532−1545

**Scheme 1. Illustration of the Synthesis of NiSx/$Cd_{0.8}Zn_{0.2}S$/rGO Nanosheet Composites by the Hydrothermal Reduction Method**

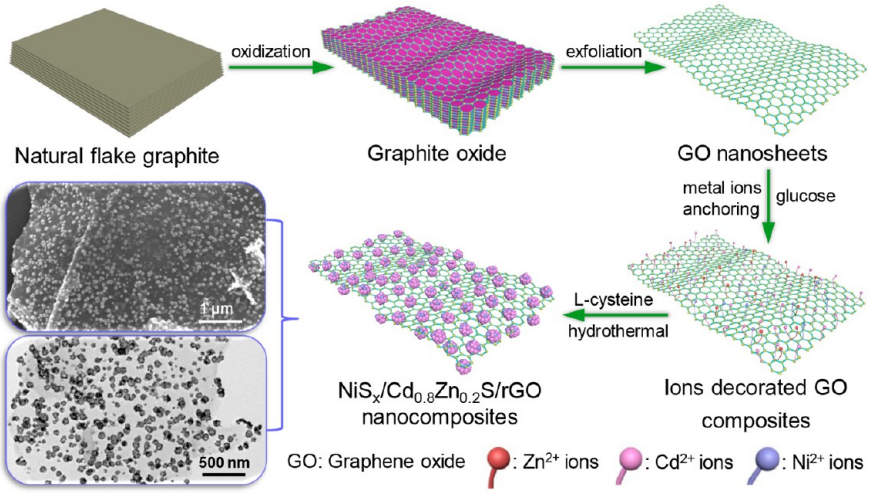


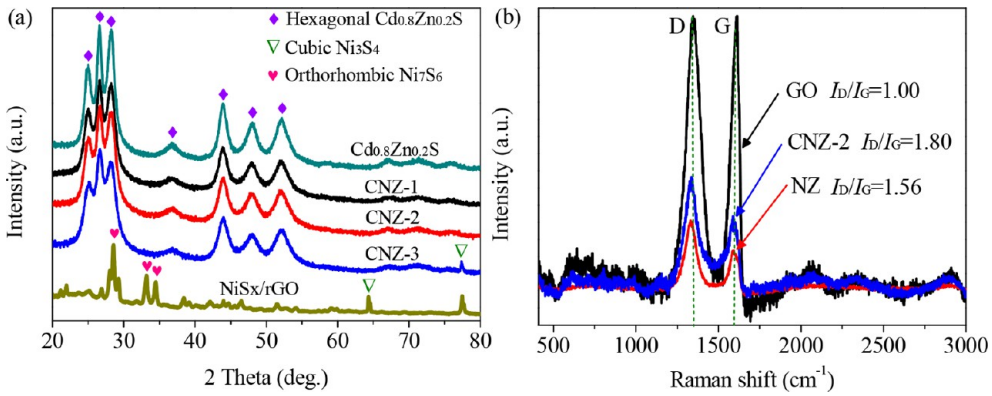


**Figure 1.** (a) XRD patterns and (b) Raman spectra of the as-fabricated samples excited at 633 nm.

3.5 m long molecular sieve 5 Å packed column with nitrogen as carrier gas) at regular intervals.

The apparent quantum efficiency (QE) was calculated under similar photocatalytic $H_2$ evolution reaction conditions. A xenon lamp (300 W, HSX-F/UV300, *NBeT*) equipped with a band-pass filter at different light wavelengths was used as a monochromatic light source. The light intensity was measured using a radiant power energy meter (FZ-A, Beijing Normal University Optical Instrument) with a calculated value of 5.5 mW $cm^{-2}$. The average hydrogen evolution rate was measured after irradiation for 5 h. The apparent QE was calculated with the equation[38]

$$\mathrm{QE}\ (\%) = \frac{\text{number of reacted electrons}}{\text{number of incident photons}} \times 100\%$$

$$= \frac{2 \times \text{number of evolved } H_2 \text{ molecules}}{\text{number of incident photons}} \times 100\%$$

**2.5. Photoelectrochemical Measurements and Characterization.** The transient photocurrent responses of the as-prepared photocatalysts were measured in a three-electrode cell by using an electrochemical station (CHI 660D, Chenhua, Shanghai, People's Republic of China). In a typical three-electrode system, a Pt wire and Ag/AgCl (immersed in the saturated KCl solution) were selected as the counter electrode and the reference electrode, respectively. During photocurrent measurements, a glassy-carbon electrode (effective area 0.071 $cm^2$) coated with photocatalyst was employed as the working electrode, which was immersed in $Na_2SO_4$ aqueous electrolyte solution (1 moL $L^{-1}$) at a static potential of 0.3 V and irradiated by visible light at regular intervals.

## 3. RESULTS AND DISCUSSION

The typical synthesis of the $Cd_{0.8}Zn_{0.2}S$/rGO nanocomposite decorated by NiSx quantum dots (QDs) is illustrated in Scheme 1. First, a modified Hummer method was employed to prepare the graphite oxide powder. To obtain monolayer or few-layer GO nanosheets with a large specific surface area, the graphite oxide precursor was treated via a liquid exfoliation process. Then, the positively charged metal ions including $Ni^{3+}$ ions, $Cd^{2+}$ ions, and $Zn^{2+}$ ions were tightly adsorbed on the negatively charged surface of GO nanosheets due to electrostatic interactions.[4,39] During the hydrothermal procedure, a zero-dimensional (0D) $Cd_{0.8}Zn_{0.2}S$ solid solution was generated and anchored homogeneously in situ on the rGO surface in the presence of the sulfur precursor L-cysteine. Meanwhile, numerous NiSx QDs cocatalysts were evenly distributed on the as-formed $Cd_{0.8}Zn_{0.2}S$/rGO nanosheet composite. It is worth noting that both L-cysteine and glucose act as reducing agents, resulting in the sufficient reduction of GO through a hydrothermal reduction strategy. For the sake of comparison, a control experiment was carried out and an NiSx/$Cd_{0.8}Zn_{0.2}S$/


DOI: 10.1021/acscatal.7b04228
ACS Catal. 2018, 8, 1532−1545

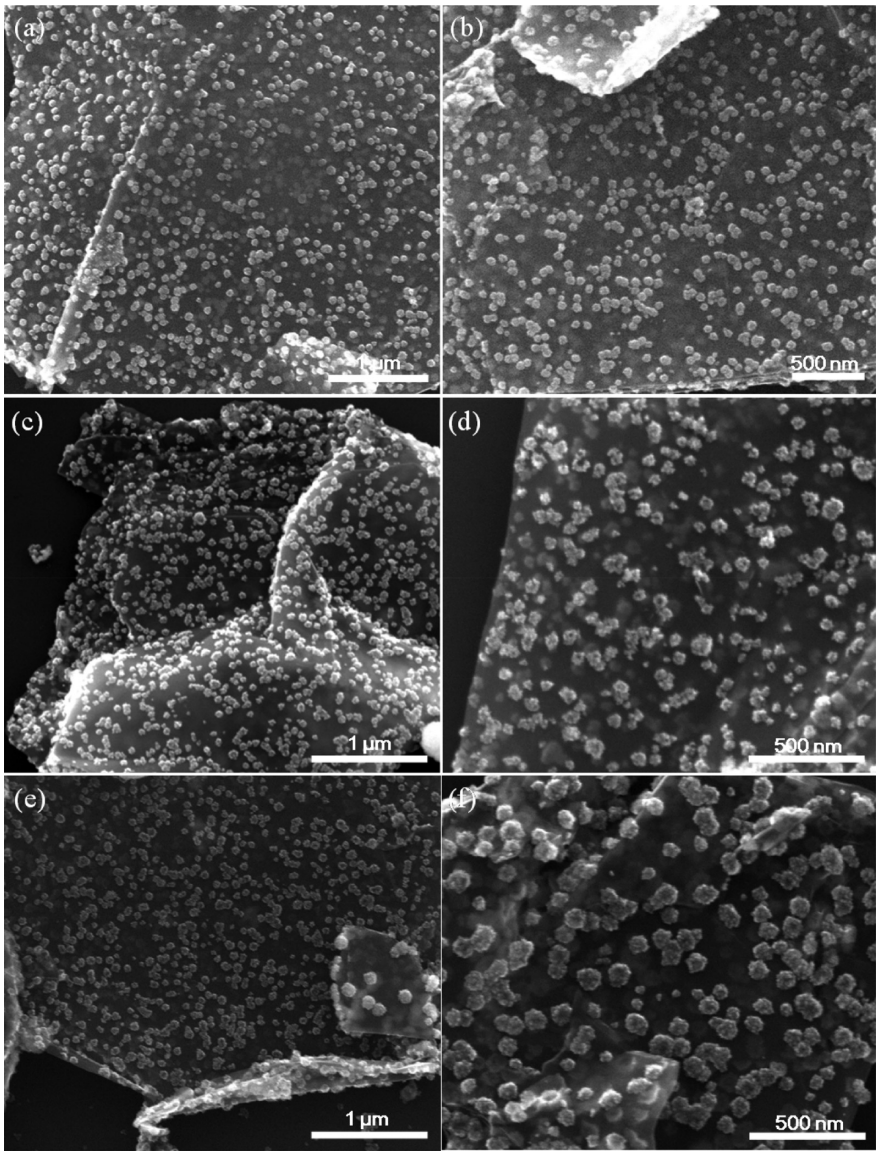


**Figure 2.** SEM images of (a, b) CNZ-1, (c, d) CNZ-2, and (e, f) CNZ-3 nanocomposites.

rGO nanosheet composite without using glucose (2 wt % NiSx, denoted NZ) was synthesized. Additionally, a series of NiSx/$Cd_{0.8}Zn_{0.2}S$/rGO nanosheet composites with different mass percentages of NiSx were prepared to investigate the influence of different amounts of cocatalyst NiSx on photocatalytic performance. The resultant samples are labeled CZ (0 wt % NiSx), CNZ-1 (1 wt % NiSx), CNZ-2 (2 wt % NiSx), and CNZ-3 (5 wt % NiSx), respectively. The overall synthetic strategy is elucidated in detail in the Experimental Section.

The formation of NiSx/$Cd_{0.8}Zn_{0.2}S$/rGO nanosheet composites is evidenced by the data of X-ray diffraction (XRD) patterns and Raman spectra. As shown in Figure 1a, two characteristic peaks at 64.4 and 77.3° in the curve of the NiSx/rGO nanocomposite can be assigned to the (533) and (137) crystal planes of cubic $Ni_3S_4$ (JCPDS No. 43-1469), respectively, while the other characteristic peaks were well-matched to the orthorhombic phase $Ni_7S_6$ (JCPDS Nos. 24-1021 and 14-0364). The XRD patterns of CNZ-1 and CNZ-2 nanocomposites are both similar to that of pure $Cd_{0.8}Zn_{0.2}S$, and all of the diffraction peaks can be well indexed to the hexagonal phase $Cd_{0.8}Zn_{0.2}S$ (JCPDS No. 49-1302). Meanwhile, no diffraction peak corresponding to NiSx can be observed due to the low amount and highly selective dispersion of the loaded NiSx. When the weight ratio of NiSx was increased to 5 wt %, the main peak at 28.4° corresponding to the (101) plane of the orthorhombic phase $Ni_7S_6$ in the CNZ-3 sample is overlapped with the diffraction peak of $Cd_{0.8}Zn_{0.2}S$. However, a remarkable diffraction peak located at 77.3° can be ascribed to the (137) plane of cubic $Ni_3S_4$, indicating that the NiSx cocatalyst materials mainly include the cubic phase $Ni_3S_4$ and orthorhombic phase $Ni_7S_6$. It should be noted that no obvious diffraction peaks for either GO or rGO can be observed in XRD patterns of the as-fabricated samples, owing to the sufficient reduction of GO to rGO during the hydrothermal process and the relatively low diffraction intensity of rGO.[40]

Nonetheless, the reduction process of GO in the nanocomposite can be confirmed by the Fourier transform infrared (FTIR) spectra. As illustrated in Figure S1, only one characteristic peak with very low intensity at 1581.05 $cm^{-1}$ can be observed over CZ, NZ, and the NiSx/$Cd_{0.8}Zn_{0.2}S$/rGO nanosheet composites, which can be well indexed to the C═O


DOI: 10.1021/acscatal.7b04228
ACS Catal. 2018, 8, 1532−1545

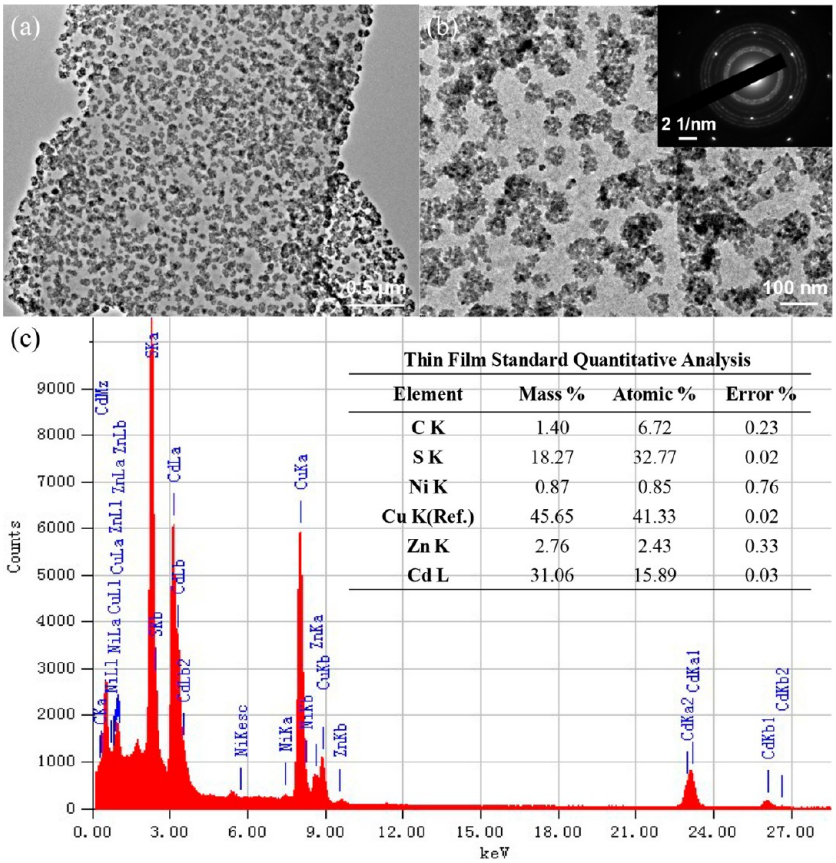


**Figure 3.** (a, b) TEM images and (c) the corresponding EDX spectrum of CNZ-2 nanocomposite. The inset of (b) gives the selected area electron diffraction (SAED) pattern.

group. In spite of this, most characteristic peaks related to the other oxygen-containing functional groups in the original GO vanished,[36] indicating that the hydrothermal treatment in the presence of the reducing agents L-cysteine and glucose led to the formation of rGO with a high reduction degree. Furthermore, Figure 1b displays a comparison of the Raman spectra of the original GO, NZ, and CNZ-2 nanocomposites. Two distinct peaks at around 1335.84 and 1588.56 $cm^{-1}$ are in good agreement with the D and G bands of graphene, respectively. The only difference is that the intensity ratio of the D band to the G band ($I_D/I_G$) for the CNZ-2 nanocomposite is 1.80, which is 1.2 and 1.8 times higher, respectively than those of the NZ nanocomposite and the original GO nanosheets.[41,42] This behavior reveals that it is not possible to obtain the highly reduced rGO nanosheets if we only choose L-cysteine as the reducing agent during the hydrothermal reduction process. As is well-known, a highly reduced rGO nanosheet with low carbon defect densities always plays a key role in improving the photocatalytic performance of the graphene-base nanocomposites.[40,43] As is demonstrated in Figure S2, the NZ nanocomposite synthesized without the addition of glucose shows an obviously decreased photocatalytic activity and the amount of $H_2$ production reaches 7.28 mmol $g^{-1}$ after 5 h of reaction, which is much lower than those of the CNZ-2 nanocomposite (39.20 mmol $g^{-1}$) and the pristine $Cd_{0.8}Zn_{0.2}S$ (23.55 mmol $g^{-1}$) under the same condition. The results of control experiments indicate that the highly reduced rGO nanosheet with low carbon defect densities and high electronic conductivity in the nanocomposites can act as an excellent electron reservoir and mediator to regulate the electronic properties and facilitate the electron interface migration. Finally, this behavior is beneficial in suppressing the recombination of the photogenerated charge carriers and prolonging the lifetime of the nanocomposite, thus significantly promoting the photocatalytic performance of $H_2$ generation.

The morphology and microstructure of the NiSx/$Cd_{0.8}Zn_{0.2}S$/rGO nanosheet composites were investigated by field-emission scanning electron microscopy (FE-SEM) and transmission electron microscopy (TEM), respectively. As displayed in the SEM images from Figure S3a,b, the as-prepared graphite oxide slabs obtained by the modified Hummer method demonstrate the characteristic layered bulk structure instead of nanosheets. Further observation from Figure S3c,d reveals that abundant 2D GO nanosheets with a smooth flat surface were obtained after successive ultrasonic exfoliation. A TEM image (Figure S3e) of GO nanosheets further discloses the wrinkle-free surface of the obtained monolayer or few-layer GO nanosheets with a large aspect ratio. Obviously, these versatile and flexible GO nanosheets with a large specific surface area, high electron mobility, and numerous oxygen-containing functional groups provide an ideal conductive platform for semiconductor loading and charge carrier migration. As is shown in Figure 2c, when the content of NiSx is 2 wt %, plenty of small NiSx/$Cd_{0.8}Zn_{0.2}S$ grains were uniformly anchored on the corrugated rGO nanosheet surface without any obvious aggregation after hydrothermal treatment. An enlarged SEM image (Figure 2d) demonstrates that most of the NiSx/$Cd_{0.8}Zn_{0.2}S$ grains have a roughly spherical structure with a diameter distribution ranging from 33 to 60 nm, which show obvious differences relative to the pristine NiSx


DOI: 10.1021/acscatal.7b04228
ACS Catal. 2018, 8, 1532−1545

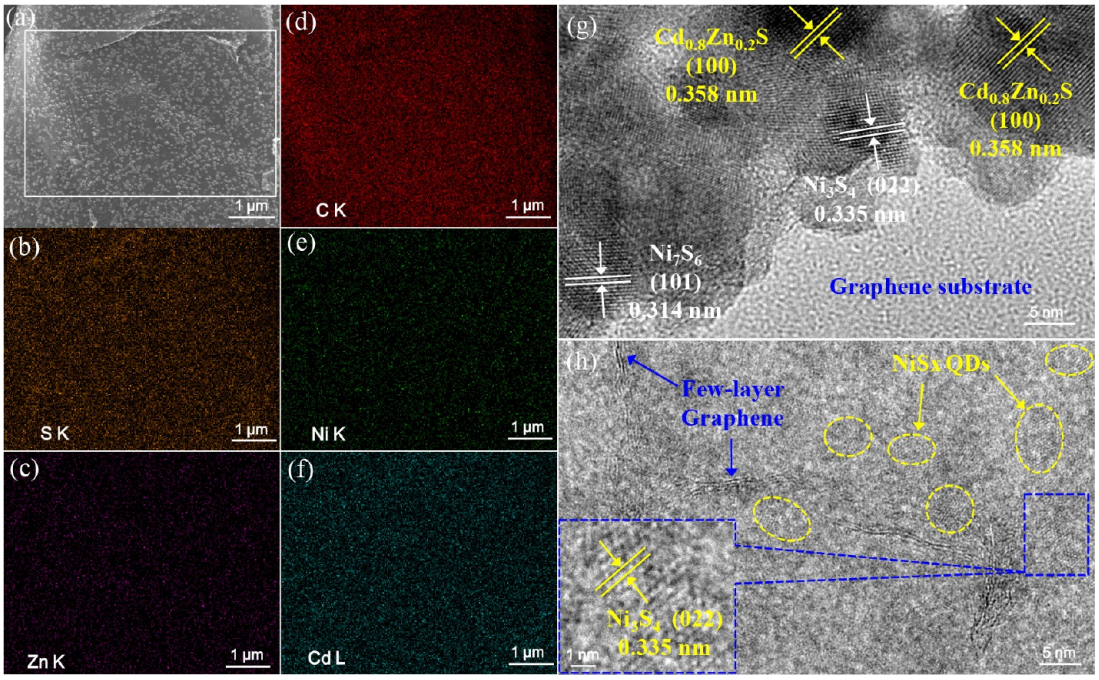


**Figure 4.** SEM image (a) and TEM images (g, h) of CNZ-2 nanocomposite and the corresponding EDX elemental mapping images of S (b), Zn (c), C (d), Ni (e), and Cd (f) in the selected area of the SEM image (a).

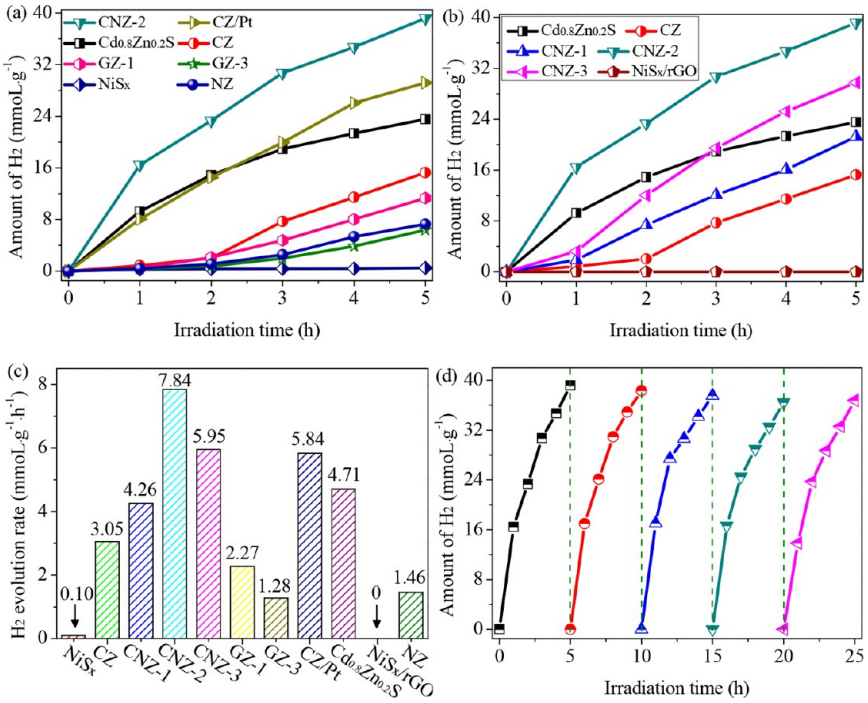


**Figure 5.** Time-dependent amounts of $H_2$ generation over photocatalysts with different amounts of (a) rGO and (b) NiSx. (c) $H_2$ evolution rates over different photocatalysts under irradiation with visible light ($\lambda$ >420 nm). (d) Recycling $H_2$ evolution over CNZ-2 nanocomposite.

nanoflakes (Figure S4a,b) and $Cd_{0.8}Zn_{0.2}S$ microspheres (Figure S4c,d). Interestingly, a decrease (Figure 2a,b; 1 wt % NiSx) or increase (Figure 2e,f; 5 wt % NiSx) in the amount of nickel sulfide has no influence on the morphology of the resultant NiSx/$Cd_{0.8}Zn_{0.2}S$/rGO nanocomposites.

In addition, TEM images in Figure 3a,b further verify the in situ planar growth of NiSx/$Cd_{0.8}Zn_{0.2}S$ nanospheres on the rGO networks. Clearly, these small-sized nanospheres are distributed homogeneously on the smooth surface of rGO, resulting in a strong interaction between rGO nanosheets and NiSx/$Cd_{0.8}Zn_{0.2}S$ nanospheres. It should be noted that the construction of intimate interfacial junctions will greatly facilitate interfacial charge transfer and migration, which is conducive to reduce the recombination efficiency of photogenerated electrons and holes, thus improving the photocatalytic performance for hydrogen production. As manifested in the inset of Figure 3b, a set of bright spots accompanied by a series of diffraction rings in the selected area electron diffraction


DOI: 10.1021/acscatal.7b04228
ACS Catal. 2018, 8, 1532−1545

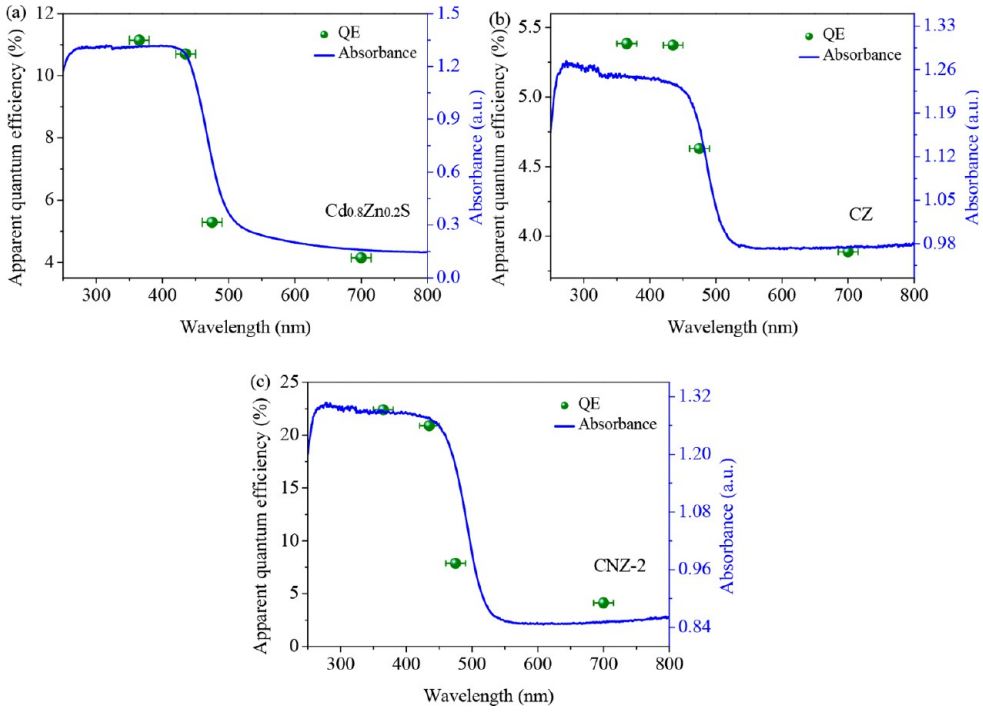


**Figure 6.** Wavelength dependence of the apparent quantum efficiencies for (a) the pure $Cd_{0.8}Zn_{0.2}S$, (b) CZ, and (c) CNZ-2 nanocomposite.

(SAED) pattern suggest the existence of few-layer rGO and the polycrystalline nature of the NiSx/$Cd_{0.8}Zn_{0.2}S$/rGO nanosheet composites.[44] The coexistence of C, Ni, Cd, Zn, and S elements in the CNZ-2 sample was proved by energy dispersive spectroscopy (EDX) (Figure 3c), implying the formation of the NiSx/$Cd_{0.8}Zn_{0.2}S$/rGO nanocomposite.

Moreover, the chemical composition of the constructed NiSx/$Cd_{0.8}Zn_{0.2}S$/rGO nanosheet composites was further detected by elemental mapping using EDX. As intuitively elucidated in Figure 4b−f, S, Zn, C, Ni, and Cd elements are uniformly distributed on the whole surface of rGO substrates. The result is consistent with the above SEM and TEM analyses. As is evident from the high-resolution transmission electron microscopy (HRTEM) images of the CNZ-2 nanocomposite, self-assembled NiSx/$Cd_{0.8}Zn_{0.2}S$ nanospheres are tightly assembled on the rGO surface with noticeable grain boundaries, forming an intimate interfacial contact with graphene (Figure 4g). Meanwhile, the lattice spacing of 0.358 nm is indexed to the (100) crystal plane of hexagonal $Cd_{0.8}Zn_{0.2}S$ (JCPDS No. 49-1302), while the other two lattice fringe spacings of 0.314 and 0.335 nm are in good agreement with the (101) plane of $Ni_7S_6$ QDs (JCPDS No. 24-1021) and the (022) plane of $Ni_3S_4$ QDs (JCPDS No. 43-1469), respectively. Additionally, few-layer rGO nanosheets can be clearly observed by an HRTEM image (Figure 4h), which possess a thickness of less than 0.83 nm.[45] In addition, the gaps generated between adjacent nanoparticles also supply a direct substrate to the host NiSx QDs. The approximate sizes of the NiSx QDs embedded within rGO are 1.8−2.4 nm. The observed lattice spacing in the inset of Figure 4h is 0.335 nm, corresponding to (022) plane of $Ni_3S_4$ QDs. It is notable that the surface of the $Cd_{0.8}Zn_{0.2}S$ was partially covered by moderate NiSx species, and the introduced accommodation sites are beneficial in the direct transfer of photoinduced electrons from $Cd_{0.8}Zn_{0.2}S$ to noble-metal-free cocatalyst NiSx QDs. Moreover, numerous monodispersed NiSx QDs are spatially confined in the graphene substrates, which undoubtedly provide sufficient catalytically active sites for efficient charge separation and fast charge transport via the close interfacial junction of $Cd_{0.8}Zn_{0.2}S$/rGO/NiSx in the hybrid.[29,46] This behavior is beneficial for enhancing their photocatalytic activities along with giving excellent stability.

The significant enhancement in the photochemical conversion efficiency over NiSx/$Cd_{0.8}Zn_{0.2}S$/rGO composites was determined distinctly and directly by visible-light-driven photocatalytic $H_2$ generation tests. As illustrated in Figure 5a, the pristine NiSx nanoflakes show negligible $H_2$ evolution under 5 h of visible-light irradiation ($\lambda \geq 420$ nm) using 10 vol % lactic acid as a sacrificial reagent, further supporting its role as a cocatalyst rather than as the main photocatalyst. Meanwhile, the pristine $Cd_{0.8}Zn_{0.2}S$ microspheres show a considerable photocatalytic activity of 23.55 mmol $g^{-1}$ under the same conditions. Nevertheless, on introduction of the rGO nanosheets in the photocatalytic system, the amount of $H_2$ evolution over $Cd_{0.8}Zn_{0.2}S$/rGO (12 wt % rGO; denoted CZ) nanosheet composite drops below 15.27 mmol $g^{-1}$, due to its "shielding effect" for hampering the light absorption.[47,48] It is amazing that, after 2 wt % of cocatalyst NiSx QDs is loaded, the photocatalytic activity of the CNZ-2 nanocomposite with 12 wt % rGO increases sharply to 39.20 mmol $g^{-1}$, which is much higher than that of the $Cd_{0.8}Zn_{0.2}S$/rGO nanosheet composite decorated by 3 wt % of the noble metal Pt (12 wt % rGO; denoted CZ/Pt; 29.18 mmol $g^{-1}$). As presented in Figure 5b, on a further decrease or increase in the loading of the non-noble-metal cocatalyst NiSx QDs, the photocatalytic $H_2$ evolution activity of NiSx/$Cd_{0.8}Zn_{0.2}S$/rGO composites is significantly changed. The corresponding amounts of $H_2$ evolution are 21.28 and 29.76 mmol $g^{-1}$ for CNZ-1 and CNZ-3 nanocomposites, respectively.

To investigate how the rGO nanosheets influence the photocatalytic activity of the nanocomposite for hydrogen evolution, we further evaluated the visible-light photocatalytic


DOI: 10.1021/acscatal.7b04228
ACS Catal. 2018, 8, 1532−1545

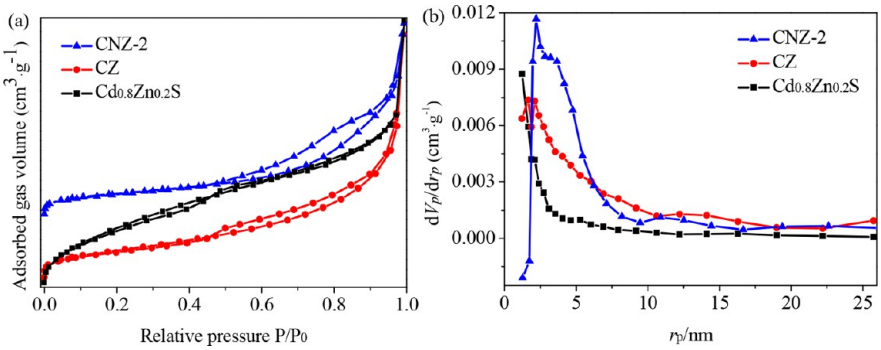


**Figure 7.** (a) $N_2$ adsorption−desorption isotherms and (b) corresponding pore-size distribution curves of the pristine $Cd_{0.8}Zn_{0.2}S$ and $Cd_{0.8}Zn_{0.2}S$/rGO and CNZ-2 nanocomposites.

$H_2$ evolution activities ($\lambda$ >420 nm) of the resultant NiSx/$Cd_{0.8}Zn_{0.2}S$/rGO nanosheet composites with different amounts of rGO. As is shown in Figure 5c, the rate of $H_2$ evolution over the CNZ-2 nanocomposite increases initially and then reaches a maximum when the amount of the rGO is about 12 wt %. It is found that the rate of $H_2$ evolution over NiSx/$Cd_{0.8}Zn_{0.2}S$/rGO nanosheet composites with 8 wt % rGO (denoted GZ-1) was measured to be 2.27 mmol $g^{-1}$ $h^{-1}$ under visible light irradiation for 5 h, which is much lower than that of the CNZ-2 nanocomposite (7.84 mmol $g^{-1}$ $h^{-1}$). This behavior can be attributed to the fact that a lower rGO loading amount leads to the aggregation of NiSx/$Cd_{0.8}Zn_{0.2}S$ particles on the surface of rGO nanosheets (Figure S5a,b), and the large particle size significantly reduces the interface contact efficiency between NiSx/$Cd_{0.8}Zn_{0.2}S$ and rGO nanosheets, thus deteriorating the photocatalytic properties of the GZ-1 nanocomposites. A further increase in the amount of rGO leads to a decrease in the $H_2$ evolution rate, and the rate of $H_2$ evolution over NiSx/$Cd_{0.8}Zn_{0.2}S$/rGO nanosheet composites with 16 wt % rGO (denoted GZ-3) was measured to be 1.28 mmol $g^{-1}$ $h^{-1}$, due to the shielding effect of the excessive loading of rGO nanosheets (Figure S5c,d).[49−51] This indicates that an appropriate rGO loading amount is capable of assisting in the photoinduced electron and hole separation at the cocatalyst/semiconductor interface, which is another key factor in achieving optimized photocatalytic activity of NiSx/$Cd_{0.8}Zn_{0.2}S$/rGO nanosheet composites.

In addition to its remarkable photocatalytic activity, the constructed $Cd_{0.8}Zn_{0.2}S$/rGO nanosheet composites decorated with 2 wt % of cocatalyst NiSx QDs also exhibit high stability. As shown in Figure 5d, no noticeable decrease in $H_2$ evolution rate can be observed even after 25 h of irradiation, confirming that NiSx QDs can serve as some of the best non-noble-metal cocatalysts for photocatalytic $H_2$ generation. We can see that the optimized CNZ-2 nanocomposite showed no apparent alterations in morphology and components (Figure S6) or in the crystal structure (Figure S7) under the same reaction conditions for five successive cycling tests in comparison with that before the photocatalytic reaction, which is in keeping with its repeated high activity for $H_2$ production.

We further measured the apparent quantum efficiencies (QEs) of the pure $Cd_{0.8}Zn_{0.2}S$, CZ, and CNZ-2 nanocomposites at different incident light wavelengths by using various band-pass filters under the same reaction conditions. As can be seen clearly from Figure 6, the trends in the wavelength dependence of the apparent QEs for all samples are similar, which closely followed those of the absorbance measured by UV−vis diffuse reflectance spectra (DRS). In addition, the apparent QE decreases markedly with an increase in wavelength, and the corresponding parameters are summarized in Table S1. Obviously, all the samples displayed extremely low apparent QEs of no more than 4.2% at 700 nm. However, the apparent QEs of photocatalytic $H_2$ evolution over the pure $Cd_{0.8}Zn_{0.2}S$ were estimated to be as high as 11.15% and 10.70% at 365 and 435 nm, respectively, which are higher than those of the CZ nanocomposite. Although the introduced rGO nanosheet cannot serve as an excellent cocatalyst or photocatalyst, it is beneficial in the enhancement of light absorption. Notably, after introduction of an appropriate amount of cocatalyst NiSx QDs (2 wt %), the CNZ-2 nanocomposite shows the highest apparent QE among these samples and the calculated values rise to 22.40% and 20.88% at 365 and 435 nm, respectively, indicating that the in situ deposited NiSx QDs are superior non-noble-metal cocatalysts for photocatalytic hydrogen evolution.

There are many factors that may affect the photocatalytic activity of the as-obtained photocatalysts. It is well-known that a high specific surface area may be beneficial for increasing surface active sites and facilitating mass transfer, thus promoting the photocatalytic activity.[32] However, for the ternary NiSx/$Cd_{0.8}Zn_{0.2}S$/rGO nanosheet composite system, this is not the case. The textural properties of the prepared samples were measured by $N_2$ adsorption−desorption isotherms. As shown in Figure 7a, three tested samples exhibit typical type IV isotherm patterns with small type H3 hysteresis loops according to the IUPAC classification, indicating the presence of slit-shaped mesopores in these nanostructures.[14,52] Moreover, Figure 7b shows the pore size distributions of all these samples, and the average pore diameters are less than 15 nm, which further verifies the existence of a well-defined mesoporous structure. The textural parameters of the three photocatalysts are presented in Table S2. Clearly, the special BET surface areas of both the $Cd_{0.8}Zn_{0.2}S$ bulk counterpart and binary $Cd_{0.8}Zn_{0.2}S$/rGO nanohybrids are estimated to be 23.76 and 25.32 $m^2$ $g^{-1}$, respectively, which are higher than that of CNZ-2 nanocomposite (18.93 $m^2$ $g^{-1}$). It can be speculated that the numerous NiSx QDs hybridized in situ with $Cd_{0.8}Zn_{0.2}S$ and graphene lead to the jamming of partial mesopores in the CNZ-2 nanocomposite and thus its special surface areas are reduced. However, the introduced NiSx QDs cocatalysts can serve as effective regulators of the electron and alternative reaction sites to improve the charge separation and surface catalytic reactions, resulting in higher photocatalytic activity.[44] This phenomenon also suggests that the remarkable


DOI: 10.1021/acscatal.7b04228
ACS Catal. 2018, 8, 1532−1545

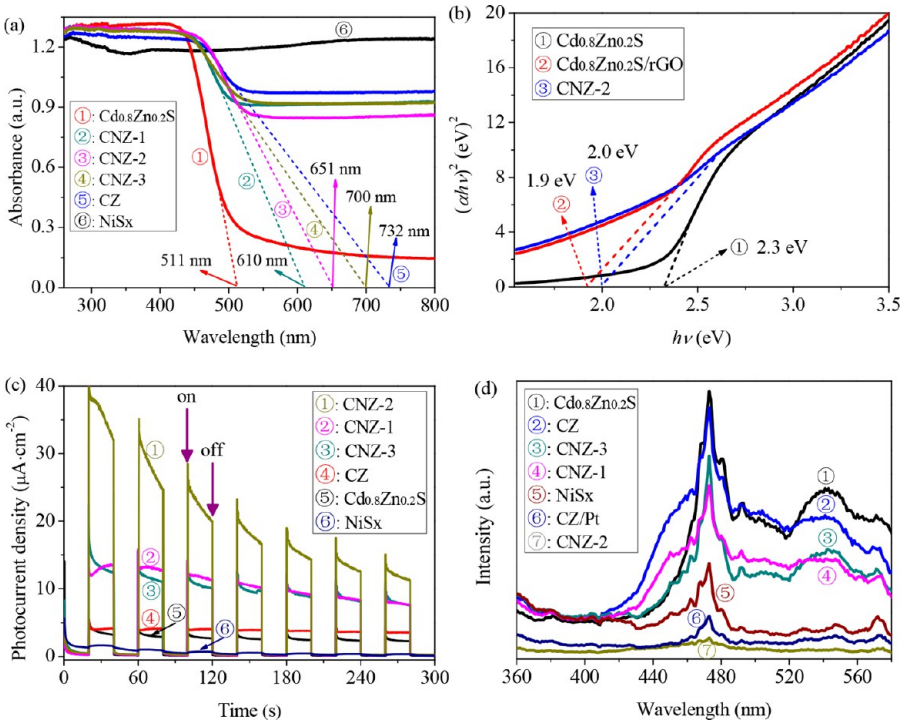


**Figure 8.** (a) UV−vis DRS spectra of all samples. (b) Tauc plots of the as-obtained samples. (c) Transient photocurrent responses. (d) Photoluminescent spectra of various photocatalysts excited at 325 nm.

photocatalytic activity enhancement of the NiSx/$Cd_{0.8}Zn_{0.2}S$/rGO nanosheet composite is not determined by changes in the specific surface area.

Furthermore, the high density of NiSx QDs cocatalysts introduced during the hydrothermal treatment also significantly alters the optical properties and electrochemical behaviors of the samples, thus directly affecting their photocatalytic activity. A comparison of the UV−vis DRS spectra in Figure 8a shows that all of the samples have an enhanced absorption in both UV- and visible-light regions as expected. The absorption edge of pure $Cd_{0.8}Zn_{0.2}S$ is up to 511 nm, corresponding to a band gap energy of 2.3 eV when $(\alpha h\nu)^2$ is used for Tauc plots (Figure 8b).[53,54] Noticeably, a distinctly enhanced absorption can be observed in the visible-light region from 500 to 800 nm after introducction of rGO and NiSx cocatalyst into the $Cd_{0.8}Zn_{0.2}S$ structure. Importantly, such a light absorption edge gradually increases with an increase in the content of NiSx cocatalyst. In comparison to the $Cd_{0.8}Zn_{0.2}S$ bulk counterpart, the absorption edges of CNZ-1, CNZ-2, and CNZ-3 nanocomposites are located at around 610, 651, and 700 nm, respectively, implying that the loaded NiSx cocatalysts simultaneously play an additional role in increasing the visible-light absorption of the resultant photocatalysts, which contributes to the enhancement of visible-light photocatalytic $H_2$ evolution activity. It is noteworthy that the absorption edges of the NiSx/$Cd_{0.8}Zn_{0.2}S$/rGO nanosheet composites exhibit slight blue shifts in comparison with that of the binary $Cd_{0.8}Zn_{0.2}S$/rGO nanocomposite (732 nm), which may be ascribed to the quantum confinement effect of NiSx QDs.[32] Accordingly, the $Cd_{0.8}Zn_{0.2}S$/rGO nanosheet composite decorated by 2 wt % of NiSx QDs still possesses the highest photocatalytic activities for hydrogen production, in spite of the fact that its light absorption wavelength is not the largest. This behavior indicates that a cocatalyst with an optimal loading amount can avoid agglomeration and reduce the "shielding effect", thus favoring the incident light absorption and generation of photoinduced charge carriers inside the internal light-harvesting center.[5,49] Moreover, an optimal NiSx QDs cocatalyst with smaller size and highly dispersed characteristic deposited in situ on the surface of semiconductors results in high interfacial contact efficiency in NiSx/rGO/$Cd_{0.8}Zn_{0.2}S$, which facilitates efficient interfacial charge transfer from the semiconductors to the cocatalysts and gives the highest activity for the visible-light-driven photocatalytic $H_2$ evolution reaction.[4]

In addition, the efficient separation and transfer of electron−hole pairs in NiSx/$Cd_{0.8}Zn_{0.2}S$/rGO nanosheet composites are also evidenced by transient photocurrent measurements and photoluminescence (PL) spectra. As elucidated in Figure 8c, it is obvious that the $Cd_{0.8}Zn_{0.2}S$/rGO nanocomposite exhibits an apparently boosted photocurrent density (4.3 $\mu$A $cm^{-2}$) in comparison to the pristine $Cd_{0.8}Zn_{0.2}S$ (3.2 $\mu$A $cm^{-2}$), indicating that the presence of graphene is beneficial to the interfacial charge separation and transfer. As expected, after the introduction of NiSx QDs, the as-prepared NiSx/$Cd_{0.8}Zn_{0.2}S$/rGO nanosheet composites exhibit higher photocurrent density in comparison to those of the pure NiSx sample and the binary $Cd_{0.8}Zn_{0.2}S$/rGO nanocomposite. In particular, the CNZ-2 nanocomposite displays the highest photocurrent response with a maximum value of 39.1 $\mu$A $cm^{-2}$ in all samples. It is believed that the synergistic effects, including the introduction of rGO nanosheets and NiSx QDs cocatalyst as well as the stronger interfacial interaction among NiSx, rGO, and $Cd_{0.8}Zn_{0.2}S$, promote the efficient interfacial transportation and separation of photogenerated electron−hole pairs, thus resulting in significantly improved photocatalytic $H_2$ production activity.[14,36,55]

In order to further deeply understand the important role of NiSx QDs cocatalysts in facilitating the transfer and separation of photogenerated charge carriers to improve the photocatalysis


DOI: 10.1021/acscatal.7b04228
ACS Catal. 2018, 8, 1532−1545

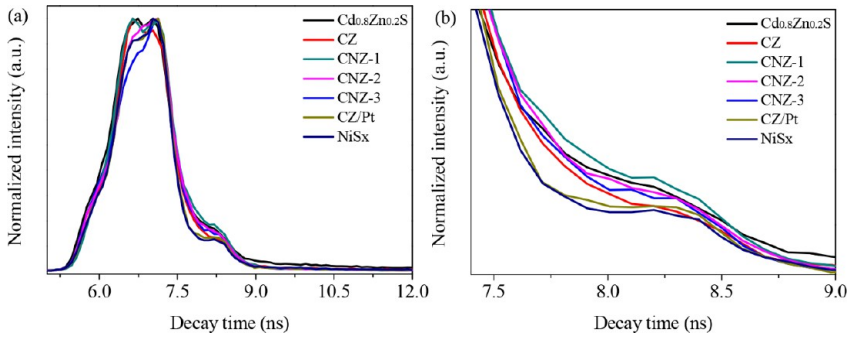


**Figure 9.** (a) Time-resolved fluorescence decay spectra of the various photocatalysts with an emission wavelength of 470 nm. (b) Partial enlargement of a portion of the spectra in (a).

**Table 1. Radiative Fluorescence Lifetimes and Relative Percentages of the Photoinduced Charge Carriers in the Various Photocatalysts**

| sample | $\tau_1$/ns | $A_1$/% | $\tau_2$/ns | $A_2$/% | $\tau_3$/ns | $A_3$/% | av lifetime $\tau$/ns |
|---|---|---|---|---|---|---|---|
| $Cd_{0.8}Zn_{0.2}S$ | 0.5024 | 65.75 | 3.4949 | 32.58 | 19.7550 | 1.67 | 5.9274 |
| CZ | 0.4342 | 82.47 | 2.8202 | 16.10 | 58.9221 | 1.43 | 30.8710 |
| CZ/Pt | 0.3604 | 81.41 | 1.7399 | 14.97 | 4.3940 | 3.62 | 1.7643 |
| NiSx | 0.3396 | 76.01 | 1.8099 | 18.16 | 4.5880 | 5.83 | 2.2355 |
| CNZ-1 | 0.4895 | 63.92 | 2.9397 | 6.80 | 1448.57 | 29.28 | 1446.823 |
| CNZ-2 | 0.4725 | 13.04 | 3.0854 | 1.71 | 1816.813 | 85.25 | 1816.679 |
| CNZ-3 | 0.4470 | 35.00 | 2.9491 | 4.14 | 1690.997 | 60.86 | 1690.54 |

efficiency of the as-prepared NiSx/$Cd_{0.8}Zn_{0.2}S$/rGO nanocomposites, the photoluminescence (PL) spectra have been used as an additionally straightforward strategy.[49] As shown in Figure 8d, the PL spectra of all the samples demonstrate that strong PL emission peaks are centered at 473 nm. In addition, the PL emission intensity of the CZ nanocomposite is comparable to that of the pure $Cd_{0.8}Zn_{0.2}S$, indicating that the presence of extra rGO nanosheets does not effectively improve the separation of photogenerated electron−hole pairs in the $Cd_{0.8}Zn_{0.2}S$/rGO nanocomposites in comparison with pure $Cd_{0.8}Zn_{0.2}S$. When NiSx was introduced into the $Cd_{0.8}Zn_{0.2}S$/rGO system, the PL emission intensities decreased dramatically. The CNZ-2 nanocomposite demonstrates the lowest emission peak intensity with respect to the other samples, including the CZ/Pt hybrid photocatalyst, suggesting the highest separation efficiency of photoinduced charge carriers. This is attributed to the fast interfacial electron transfer from the light-trapping center $Cd_{0.8}Zn_{0.2}S$ to the surface reaction site NiSx QDs through the rGO networks when the amount of the loading of NiSx reaches an optimum (about 2 wt %).[36] It is notable that the PL spectra analyses are also consistent with the transient photocurrent measurements, as mentioned above.

The improved efficiency in the transfer of charge carriers was further investigated by time-resolved fluorescence decay spectra with an emission wavelength of 470 nm. As displayed in Figure 9a, the spectra of the as-synthesized photocatalysts are well fit to a triexponential decay model. The decay parameters obtained from time-resolved fluorescence decay curves are summarized in Table 1. It can be seen that the triexponential fitted decay curves of all the samples can be characterized by a fast decay component with amplitudes $A_1$ and $A_2$ and lifetimes $\tau_1$ and $\tau_2$, respectively, related to the fast recombination of excitons, and a relatively long-lasting decay component with amplitude $A_3$ and lifetime $\tau_3$. Of note, the average lifetime $\tau$ for the as-prepared samples is calculated by the formula $\tau = (A_1\tau_1^2 + A_2\tau_2^2 + A_3\tau_3^2)/(A_1\tau_1 + A_2\tau_2 + A_3\tau_3)$.[56] As displayed in Table 1, the pristine NiSx and CZ/Pt nanocomposite show a very fast relaxation. The PL lifetimes of these two samples are very short, no more than 3 ns, indicating an ultrafast recombination of the photogenerated charge carriers. In addition, the pure $Cd_{0.8}Zn_{0.2}S$ and CZ nanocomposite exhibit prolonged PL decay lifetimes (for $Cd_{0.8}Zn_{0.2}S$, $\tau$ = 5.9274 ns; for CZ nanocomposite, $\tau$ = 30.8710 ns). Both the short lifetime ($\tau_1$ and $\tau_2$) and the long lifetime ($\tau_3$) of the charge carriers for the two aforementioned samples have increased slightly in comparison to those of the pristine NiSx and CZ/Pt nanocomposite. Most interestingly, we found that the introduction of NiSx leads to a significant improvement in the PL decay lifetime in the as-prepared NiSx/$Cd_{0.8}Zn_{0.2}S$/rGO nanocomposite. For CNZ-1, CNZ-2, and CNZ-3 nanocomposites, in the first several nanoseconds rapid recombination of the photoinduced charge carriers occurs in $Cd_{0.8}Zn_{0.2}S$, resulting in a fast PL decay ($\tau_1$ and $\tau_2$). However, their PL decay associated with the long-lasting decay component ($A_3$ and $\tau_3$) is markedly different, depending on the amount of the loading of NiSx. The differences in the samples with regard to the PL decay behavior can be clearly seen from a partial enlargement of the time-resolved fluorescence decay spectra (Figure 9b). Obviously, the long-lasting decay components ($A_3$ = 85.25% and $\tau_3$ = 1816.813 ns) for the CNZ-2 nanocomposite are much larger than those of the CNZ-1 ($A_3$ = 29.28% and $\tau_3$ = 1448.57 ns) and CNZ-3 nanocomposites ($A_3$ = 60.86% and $\tau_3$ = 1690.997 ns), respectively. The long-lifetime ($\tau_3$) process is much slower than the short-lifetime ($\tau_1$ and $\tau_2$) process and accounts for a large fraction of the PL decay lifetime. As a result, the CNZ-2 nanocomposite displays the maximum PL decay lifetime ($\tau$ = 1816.679 ns) of all the samples. This result indicates that the presence of an appropriate amount of NiSx cocatalyst and rGO nanosheet "bridge" can significantly facilitate the spatial separation and migration of interfacial photogenerated electron−hole pairs, resulting in a markedly


DOI: 10.1021/acscatal.7b04228
ACS Catal. 2018, 8, 1532−1545

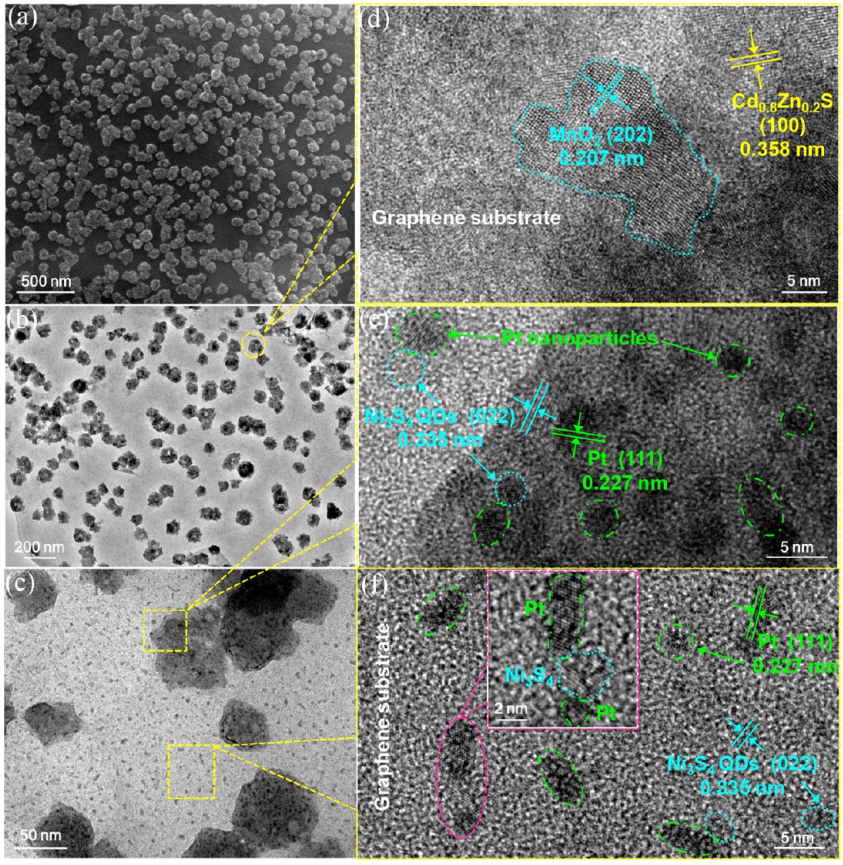


**Figure 10.** (a) SEM, (b) TEM, and (c–f) HRTEM images of CNZ-2 nanocomposite with simultaneously photodeposited MnOx and Pt nanoparticles. The contents of deposited MnOx and Pt are 8 and 3 wt %, respectively.

prolonged radiative lifetime of charge carriers, thus effectively improving the photocatalytic $H_2$ evolution performance.

We sought to clarify how the interfacial charge carriers transfer and separate between the different interfaces of the as-prepared NiSx/$Cd_{0.8}Zn_{0.2}S$/rGO nanosheet composites during the photocatalytic hydrogen production process. To this end, simultaneous photo-oxidation deposition of MnOx nanoparticles and photoreduction deposition of Pt nanoparticles was performed.[57,58] As can be seen from the SEM image (Figure 10a) and TEM image (Figure 10b) of CNZ-2 nanocomposite with simultaneously photodeposited MnOx and Pt nanoparticles, there are no apparent changes in the surface morphologies in comparison to the original CNZ-2 nanocomposite mentioned above. However, the HRTEM results clearly confirm the successful loading of the metallic Pt nanoparticles and MnOx components onto the NiSx/$Cd_{0.8}Zn_{0.2}S$/rGO nanosheet composites. As presented in Figure 10c and Figure S8a,b, the surfaces of NiSx/$Cd_{0.8}Zn_{0.2}S$ nanospheres located on the rGO nanosheets have been covered with a layer of relatively dense substances. Obviously, the obtained "island-like" nanocomposites demonstrate an extended diameter ranging from 72 to 104 nm in comparison with that of the original NiSx/$Cd_{0.8}Zn_{0.2}S$ nanospheres presented in Figure 3b. HRTEM images (Figure 10d and Figure S8d) clearly show that the MnOx nanoparticles are solely photo-oxidation deposited on the $Cd_{0.8}Zn_{0.2}S$ surfaces. Meanwhile, the heterointerface near the boundary of $Cd_{0.8}Zn_{0.2}S$ nanospheres displayed two lattice fringes with interplanar distances of 0.358 and 0.207 nm, corresponding to the (100) plane of $Cd_{0.8}Zn_{0.2}S$ and (202) plane of $MnO_2$, respectively. Further observation reveals that the smaller sized Pt nanoparticles have been successfully photoreduced and randomly distributed on the surfaces of both NiSx/$Cd_{0.8}Zn_{0.2}S$ nanospheres (Figure 10e and Figure S8c,d) and NiSx/rGO substrate (Figure 10f and Figure S8e,f) with a diameter of less than 2 nm. The lattice fringes with spacings of 0.335 and 0.227 nm can be assigned to the (022) and (111) planes of $Ni_3S_4$ and Pt, respectively. More importantly, the EDX spectrum (Figure S9a) and the XRD patterns (Figure S9b) further confirm that the CNZ-2 nanocomposite after simultaneous photodepositing of MnOx and Pt nanoparticles contains the obvious signals of C, O, Ni, Zn, Pt, Mn, Cd, and S elements. The photodeposited MnOx species consist of orthorhombic $MnO_2$, $Mn_2O_3$, and tetragonal $Mn_3O_4$. All of the above characterization results evidence that the photo-oxidation deposition of MnOx nanoparticles selectively took place only on the positively charged surfaces of $Cd_{0.8}Zn_{0.2}S$ solid solution nanospheres, while photoreduction deposition of Pt nanoparticles occurred simultaneously on the negatively charged surface of NiSx/$Cd_{0.8}Zn_{0.2}S$ nanospheres and NiSx/rGO substrate. This behavior indicates that rGO nanosheets are extremely important 2D conducting substrates, which can accelerate the interfacial electron transfer from $Cd_{0.8}Zn_{0.2}S$ to NiSx QDs cocatalysts via the rGO network,[59,60] thus contributing to the enhancement in the efficiency of the visible-light-driven photocatalytic $H_2$ generation reaction.

On the basis of the aforementioned characterization analyses and experimental results, a convincing mechanism illustrating the surprisingly high photocatalytic $H_2$ production activity of the NiSx/$Cd_{0.8}Zn_{0.2}S$/rGO nanocomposites (2 wt %) is given


DOI: 10.1021/acscatal.7b04228
ACS Catal. 2018, 8, 1532−1545

in Scheme 2. Under visible-light irradiation, the uncovered solid solution surface can effectively adsorb visible light, due to its outstanding visible-light response ability. In addition, the photogenerated electrons are excited from the valence band of $Cd_{0.8}Zn_{0.2}S$ solid solution nanospheres to its conduction band. As mentioned, two distinctive growth pathways of NiSx QDs will cause the diverse surface electron redistribution in the NiSx/$Cd_{0.8}Zn_{0.2}S$/rGO composite system. For route I, the eutectic clusters consisting of a part of the NiSx QDs and $Cd_{0.8}Zn_{0.2}S$ nanocrystals were self-assembled into mesoporous NiSx/$Cd_{0.8}Zn_{0.2}S$ nanospheres, which anchored in situ on the rGO nanosheets. Notably, this mesoporous nanoarchitecture is beneficial for solution infiltration and adsorption.[61] The intimate contacts between the two nearest neighboring NiSx QDs and $Cd_{0.8}Zn_{0.2}S$ nanocrystals shorten the path of electron transfer and lead to the directly photogenerated electron transfer from $Cd_{0.8}Zn_{0.2}S$ to the cocatalyst NiSx QDs, accompanying the elimination of photogenerated holes by lactic acid scavengers. Therefore, through tuning the loading amount of cocatalyst NiSx QDs on the surface of $Cd_{0.8}Zn_{0.2}S$ solid solution, one can achieve desirable results for enlarging the light-harvesting efficiency, suppressing the rapid recombination of photoexcited electrons and holes during long-distance transportation between the separated photoabsorbers and reaction centers,[33] thus optimizing the photocatalytic $H_2$ evolution activities. For route II, the in-plane heterostructure of NiSx/rGO and $Cd_{0.8}Zn_{0.2}S$/rGO nanohybrids favors the photocatalytic hydrogen evolution reaction. It is evident that the quantum-sized NiSx can be easily and uniformly anchored on the surface of rGO nanosheets. One important advantage of this construction is that the individual NiSx QDs not only can provide more exposed active sites for hydrogen evolution reaction but also can be combined readily with surface-adsorbed $H_2O$ to form Ni−H bonds during proton reduction.[19] Although the introduced rGO substrates and NiSx QDs do not contribute to the generation of photoinduced carriers, the 2D rGO nanosheets with excellent electrical conductivity can serve as huge reservoirs of electrons for facilitating fast charge transfer.[49] Therefore, a large portion of photoinduced electrons will rapidly shuttle from $Cd_{0.8}Zn_{0.2}S$ nanocrystals to the surface of isolated catalytically active sites of NiSx QDs through the "bridge" of rGO nanosheets, due to its zero energy gap.[41,62] Then the enriched electrons on $H_2O$-bonded NiSx QDs will react with adsorbed $H^+$ ions to generate $H_2$ at lower overpotential, which further imposes a pronounced synergetic enhancement effect on the photocatalytic activity and stability of the NiSx/$Cd_{0.8}Zn_{0.2}S$/rGO nanohybrid system. In this interpretation, the combined effects of the introduction of moderate rGO nanosheets and the optimization of NiSx QDs loading in this unique nanoarchitecture are indeed crucially important for surface electronic structure modification and ultrafast spatial transfer and separation of interfacial photogenerated electron−hole pairs, which remarkably improve the efficiency of solar light utilization and water splitting for $H_2$ generation.

**Scheme 2. Illustration of the Possible Charge Transfer and Cocatalytic Mechanism of $H_2$ Generation in the NiSx/$Cd_{0.8}Zn_{0.2}S$/rGO Composite system**

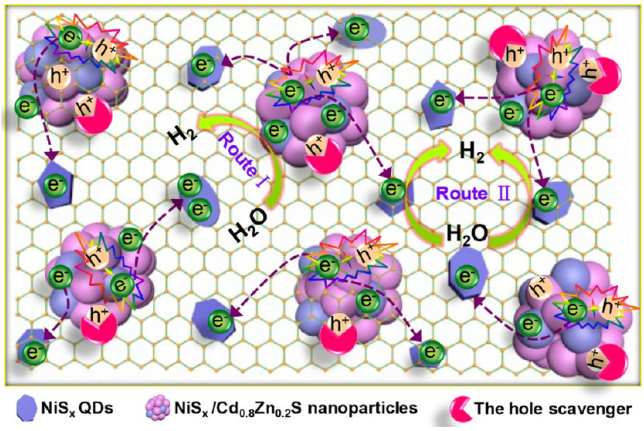


## 4. CONCLUSIONS

In summary, we have successfully synthesized a novel NiSx/$Cd_{0.8}Zn_{0.2}S$/rGO nanohybrid by a facile hydrothermal strategy. The well-defined $Cd_{0.8}Zn_{0.2}S$ solid solution nanospheres were in-plane epitaxially grown on the rGO nanosheet surfaces, accompanied by the in situ deposition of NiSx QDs on the surfaces of both $Cd_{0.8}Zn_{0.2}S$ and rGO. The introduction of a conductive rGO substrate provides a universal interface engineering strategy for the construction of an interfacial connection of the heterostructure. More importantly, the incorporation of high-density noble-metal-free NiSx cocatalysts (2 wt %) not only increases the exposure of active sites but also significantly alters the surface electron distribution. The synergistic effects not only improve light-harvesting ability but also benefit the rapid spatial transfer and separation of interfacial photogenerated electron−hole pairs, resulting in remarkable $H_2$ production with a rate of 7.84 mmol $g^{-1}$ $h^{-1}$ and an apparent QE of 20.88% (435 nm) under visible-light irradiation. The new electron transfer mechanism derived from the multiple coupling manners of NiSx QDs provides a new scenario for cocatalyst design, which is able to replace noble metals in practical applications of solar water splitting for $H_2$ evolution.

## ■ ASSOCIATED CONTENT

### Supporting Information

The Supporting Information is available free of charge on the ACS Publications website at DOI: 10.1021/acscatal.7b04228.

FT-IR spectra of the as-prepared samples, TEM images of GO and CNZ-2 nanocomposite after photocatalytic reaction for 5 and 25 h, SEM image of the pristine NiSx nanoflakes, the pure $Cd_{0.8}Zn_{0.2}S$ microspheres, and CNZ-1 and CNZ-3 nanocomposites, summary of BET surface areas ($S_{BET}$), pore volumes ($V_p$), and average pore diameters ($D_p$) of the as-synthesized photocatalysts, EDX spectra of CNZ-2 nanocomposite after a five-cycle test and CNZ-2 nanocomposite with simultaneously photodeposited MnOx and Pt nanoparticles, and XRD patterns of original CNZ-2 nanocomposite, CNZ-2 nanocomposite after a five-cycle test, and CNZ-2 nanocomposite with simultaneously photodeposited MnOx and Pt nanoparticles (PDF)

## ■ AUTHOR INFORMATION

**Corresponding Author**

*E-mail for G.Y.: guidongyang@xjtu.edu.cn.

**ORCID**

Bolun Yang: 0000-0003-0340-4871

Guidong Yang: 0000-0001-6629-1312



DOI: 10.1021/acscatal.7b04228
ACS Catal. 2018, 8, 1532−1545

### Notes

The authors declare no competing financial interest.

## ■ ACKNOWLEDGMENTS

This work was financially supported by the Natural Science Basic Research Plan in Shaanxi Province of China (Grant No. 2017JZ001), the National Natural Science Foundation of China (Grant No. 21303130), the State Key Laboratory of Heavy Oil Processing (SKLOP201602001), the Fundamental Research Funds for the Central Universities (Grant No. cxtd2017004), and the K. C. Wong Education Foundation, Hong Kong, People's Republic of China. We acknowledge technical support from the International Center for Dielectric Research (ICDR), Xi'an Jiaotong University, Xi'an, People's Republic of China; the authors also thank Ms. Dai and Mr. Ma for their help in using SEM and EDX and TEM, respectively.

## ■ REFERENCES

(1) Maeda, K.; Teramura, K.; Lu, D.; Takata, T.; Saito, N.; Inoue, Y.; Domen, K. *Nature* **2006**, *440*, 295−296.
(2) Wu, F.; Liao, Q.; Cao, F.; Li, L.; Zhang, Y. *Nano Energy* **2017**, *34*, 8−14.
(3) Yang, L.; Zhou, W.; Lu, J.; Hou, D.; Ke, Y.; Li, G.; Tang, Z.; Kang, X.; Chen, S. *Nano Energy* **2016**, *22*, 490−498.
(4) Kong, C.; Min, S.; Lu, G. *ACS Catal.* **2014**, *4*, 2763−2769.
(5) Ran, J.; Zhang, J.; Yu, J.; Jaroniec, M.; Qiao, S. Z. *Chem. Soc. Rev.* **2014**, *43*, 7787−7812.
(6) Lin, B.; An, H.; Yan, X.; Zhang, T.; Wei, J.; Yang, G. *Appl. Catal., B* **2017**, *210*, 173−183.
(7) Niu, F.; Dong, C.-L.; Zhu, C.; Huang, Y.-C.; Wang, M.; Maier, J.; Yu, Y.; Shen, S. *J. Catal.* **2017**, *352*, 35−41.
(8) Zong, X.; Yan, H.; Wu, G.; Ma, G.; Wen, F.; Wang, L.; Li, C. *J. Am. Chem. Soc.* **2008**, *130*, 7176−7177.
(9) Wei, L.; Chen, Y.; Lin, Y.; Wu, H.; Yuan, R.; Li, Z. *Appl. Catal., B* **2014**, *144*, 521−527.
(10) Xiang, Q.; Yu, J.; Jaroniec, M. *J. Am. Chem. Soc.* **2012**, *134*, 6575−6578.
(11) Zhong, Y.; Shao, Y.; Ma, F.; Wu, Y.; Huang, B.; Hao, X. *Nano Energy* **2017**, *31*, 84−89.
(12) Hou, Y.; Zhu, Y.; Xu, Y.; Wang, X. *Appl. Catal., B* **2014**, *156−157*, 122−127.
(13) Chen, J.; Wu, X.-J.; Yin, L.; Li, B.; Hong, X.; Fan, Z.; Chen, B.; Xue, C.; Zhang, H. *Angew. Chem., Int. Ed.* **2015**, *54*, 1210−1214.
(14) Yuan, J. L.; Wen, J.; Zhong, Y.; Li, X.; Fang, Y.; Zhang, S.; Liu, W. *J. Mater. Chem. A* **2015**, *3*, 18244−18255.
(15) Zhang, J.; Liu, Z.; Liu, Z. *ACS Appl. Mater. Interfaces* **2016**, *8*, 9684−9691.
(16) Lei, Y.; Pakhira, S.; Fujisawa, K.; Wang, X.; Iyiola, O. O.; López, N. P.; Elías, A. L.; Rajukumar, L. P.; Zhou, C.; Kabius, B.; Alem, N.; Endo, M.; Lv, R.; Mendoza-Cortes, J. L.; Terrones, M. *ACS Nano* **2017**, *11*, 5103−5112.
(17) Wang, L.; Wu, X.; Guo, S.; Han, M.; Zhou, Y.; Sun, Y.; Huang, H.; Liu, Y.; Kang, Z. *J. Mater. Chem. A* **2017**, *5*, 2717−2723.
(18) Wang, Z.; Peng, J.; Feng, X.; Ding, Z.; Li, Z. *Catal. Sci. Technol.* **2017**, *7*, 2524−2530.
(19) Liu, M.; Chen, Y.; Su, J.; Shi, J.; Wang, X.; Guo, L. *Nat. Energy* **2016**, *1*, 16151.
(20) Kobosko, S. M.; Jara, H. D.; Kamat, P. V. *ACS Appl. Mater. Interfaces* **2017**, *9*, 33379−33388.
(21) Yang, Y.; Tang, D.-M.; Zhang, C.; Zhang, Y.; Liang, Q.; Chen, S.; Weng, Q.; Zhou, M.; Xue, Y.; Liu, J. W.; Wu, J.; Cui, Q. H.; Lian, C.; Hou, G.; Yuan, F.; Bando, Y.; Golberg, D.; Wang, X. *Energy Environ. Sci.* **2017**, *10*, 979−986.
(22) Kim, J.; Cote, L. J.; Huang, J. *Acc. Chem. Res.* **2012**, *45*, 1356−1364.
(23) Tan, C.; Cao, X.; Wu, X.-J.; He, Q.; Yang, J.; Zhang, X.; Chen, J.; Zhao, W.; Han, S.; Nam, G.-H.; Sindoro, M.; Zhang, H. *Chem. Rev.* **2017**, *117*, 6225−6331.
(24) Zhang, S.; Huang, Z.; Wen, Z.; Zhang, L.; Jin, J.; Shahbazian-Yassar, R.; Yang, J. *Nano Lett.* **2017**, *17*, 3518−3526.
(25) Tan, C.; Zhang, H. *J. Am. Chem. Soc.* **2015**, *137*, 12162−12174.
(26) Song, J.; Zhao, H.; Sun, R.; Li, X.; Sun, D. *Energy Environ. Sci.* **2017**, *10*, 225−235.
(27) Liu, M.; Jing, D.; Zhou, Z.; Guo, L. *Nat. Commun.* **2013**, *4*, 2278.
(28) Mei, Z.; Zhang, B.; Zheng, J.; Yuan, S.; Zhuo, Z.; Meng, X.; Chen, Z.; Amine, K.; Yang, W.; Wang, L.-W.; Wang, W.; Wang, S.; Gong, Q.; Li, J.; Liu, F.-S.; Pan, F. *Nano Energy* **2016**, *26*, 405−416.
(29) Du, R.; Zhang, Y.; Li, B.; Yu, X.; Liu, H.; An, X.; Qu, J. *Phys. Chem. Chem. Phys.* **2016**, *18*, 16208−16215.
(30) De, S.; Zhang, J.; Luque, R.; Yan, N. *Energy Environ. Sci.* **2016**, *9*, 3314−3347.
(31) Wu, J.; Wang, L.; Lv, B.; Chen, J. *ACS Appl. Mater. Interfaces* **2017**, *9*, 14319−14327.
(32) Li, Y.; Jin, R.; Xing, Y.; Li, J.; Song, S.; Liu, X.; Li, M.; Jin, R. *Adv. Energy Mater.* **2016**, *6*, 1601273.
(33) Che, W.; Cheng, W.; Yao, T.; Tang, F.; Liu, W.; Su, H.; Huang, Y.; Liu, Q.; Liu, J.; Hu, F.; Pan, Z.; Sun, Z.; Wei, S. *J. Am. Chem. Soc.* **2017**, *139*, 3021−3026.
(34) Liu, X.; Iocozzia, J.; Wang, Y.; Cui, X.; Chen, Y.; Zhao, S.; Li, Z.; Lin, Z. *Energy Environ. Sci.* **2017**, *10*, 402−434.
(35) Hou, Y.; Wen, Z.; Cui, S.; Feng, X.; Chen, J. *Nano Lett.* **2016**, *16*, 2268−2277.
(36) Han, Q.; Wang, B.; Gao, J.; Cheng, Z. H.; Zhao, Y.; Zhang, Z. P.; Qu, L. T. *ACS Nano* **2016**, *10*, 2745−2751.
(37) Han, X.-W.; Meng, X.-Z.; Zhang, J.; Wang, J.-X.; Huang, H.-F.; Zeng, X.-F.; Chen, J.-F. *Ind. Eng. Chem. Res.* **2016**, *55*, 11622−11630.
(38) Hai, X.; Chang, K.; Pang, H.; Li, M.; Li, P.; Liu, H.; Shi, L.; Ye, J. *J. Am. Chem. Soc.* **2016**, *138*, 14962−14969.
(39) Han, X.; Yu, C.; Zhou, S.; Zhao, C.; Huang, H.; Yang, J.; Liu, Z.; Zhao, J.; Qiu, J. *Adv. Energy Mater.* **2017**, *7*, 1602148.
(40) Chen, Y.; Ge, H.; Wei, L.; Li, Z.; Yuan, R.; Liu, P.; Fu, X. *Catal. Sci. Technol.* **2013**, *3*, 1712−1717.
(41) Yu, X.; Zhang, J.; Zhao, Z.; Guo, W.; Qiu, J.; Mou, X.; Li, A.; Claverie, J. P.; Liu, H. *Nano Energy* **2015**, *16*, 207−217.
(42) Zhang, Z.; Gao, C.; Li, Y.; Han, W.; Fu, W.; He, Y.; Xie, E. *Nano Energy* **2016**, *30*, 892−899.
(43) Ye, L.; Fu, J.; Xu, Z.; Yuan, R.; Li, Z. *ACS Appl. Mater. Interfaces* **2014**, *6*, 3483−3490.
(44) Zhang, G.; Lan, Z.-A.; Lin, L.; Lin, S.; Wang, X. *Chem. Sci.* **2016**, *7*, 3062−3066.
(45) Lei, F.; Liu, W.; Sun, Y.; Xu, J.; Liu, K.; Liang, L.; Yao, T.; Pan, B.; Wei, S.; Xie, Y. *Nat. Commun.* **2016**, *7*, 12697.
(46) Ji, K. M.; Arandiyan, H.; Liu, P.; Zhang, L.; Han, J.; Xue, Y.; Hou, J.; Dai, H. *Nano Energy* **2016**, *27*, 515−525.
(47) Li, L.; Deng, Z.; Yu, L.; Lin, Z.; Wang, W.; Yang, G. *Nano Energy* **2016**, *27*, 103−113.
(48) Zhang, J.; Li, W.; Li, Y.; Zhong, L.; Xu, C. *Appl. Catal., B* **2017**, *217*, 30−36.
(49) Ran, J.; Gao, G.; Li, F.-T.; Ma, T.-Y.; Du, A.; Qiao, S.-Z. *Nat. Commun.* **2017**, *8*, 13907.
(50) Yu, H.; Shi, R.; Zhao, Y.; Bian, T.; Zhao, Y.; Zhou, C.; Waterhouse, G. I. N.; Wu, L.-Z.; Tung, C.-H.; Zhang, T. *Adv. Mater.* **2017**, *29*, 1605148.
(51) Latorre-Sanchez, M.; Primo, A.; Garcia, H. *Angew. Chem., Int. Ed.* **2013**, *52*, 11813−11816.
(52) Xue, C.; Wang, T.; Yang, G.; Yang, B.; Ding, S. *J. Mater. Chem. A* **2014**, *2*, 7674−7679.
(53) Zhang, Z.; Gao, C.; Wu, Z.; Han, W.; Wang, Y.; Fu, W.; Li, X.; Xie, E. *Nano Energy* **2016**, *19*, 318−327.
(54) Han, J.; Liu, Z.; Guo, K.; Wang, B.; Zhang, X.; Hong, T. *Appl. Catal., B* **2015**, *163*, 179−188.
(55) Wang, B.; Liu, Z.; Han, J.; Hong, T.; Zhang, J.; Li, Y.; Cui, T. *Electrochim. Acta* **2015**, *176*, 334−343.


DOI: 10.1021/acscatal.7b04228
*ACS Catal.* 2018, 8, 1532−1545

(56) Tu, W.; Li, Y.; Kuai, L.; Zhou, Y.; Xu, Q.; Li, H.; Wang, X.; Xiao, M.; Zou, Z. *Nanoscale* **2017**, *9*, 9065−9070.
(57) Shi, R.; Cao, Y.; Bao, Y.; Zhao, Y.; Waterhouse, G. N.; Fang, Z.; Wu, L.-Z.; Tung, C.-H.; Yin, Y.; Zhang, T. *Adv. Mater.* **2017**, *29*, 1700803.
(58) Li, R.; Zhang, F.; Wang, D.; Yang, J.; Li, M.; Zhu, J.; Zhou, X.; Han, H.; Li, C. *Nat. Commun.* **2013**, *4*, 1432.
(59) Xu, X.; Nosheen, F.; Wang, X. *Chem. Mater.* **2016**, *28*, 6313−6320.
(60) Argentero, G.; Mittelberger, A.; Monazam, M. R. A.; Cao, Y.; Pennycook, T. J.; Mangler, C.; Kramberger, C.; Kotakoski, J.; Geim, A. K.; Meyer, J. C. *Nano Lett.* **2017**, *17*, 1409−1416.
(61) Chang, K.; Mei, Z.; Wang, T.; Kang, Q.; Ouyang, S.; Ye, J. *ACS Nano* **2014**, *8*, 7078−7087.
(62) Xue, C.; An, H.; Yan, X.; Li, J.; Yang, B.; Wei, J.; Yang, G. *Nano Energy* **2017**, *39*, 513−523.



DOI: 10.1021/acscatal.7b04228
*ACS Catal.* 2018, 8, 1532−1545